Modulation of single atomic Co and Fe sites on hollow carbon nanospheres as oxygen electrodes for rechargeable Zn–air batteries

Jose, Vishal; Hu, Huimin; Edison, Eldho; Manalastas, William, Jr.; Ren, Hao; Kidkhunthod, Pinit; Sreejith, Sivaramapanicker; Jayakumar, Anjali; Nsanzimana, Jean Marie Vianney; Srinivasan, Madhavi; Choi, Jinho; Lee, Jong-Min

2021

https://hdl.handle.net/10356/147555

https://doi.org/10.1002/smtd.202000751

Modulation of Single Atomic Co and Fe Sites on Hollow Carbon Nanospheres as Oxygen Electrodes for Rechargeable Zn–Air Batteries

Vishal Jose, Huimin Hu, Eldho Edison, William Manalastas Jr., Hao Ren, Pinit Kidkhunthod, Sivaramapanicker Sreejith, Anjali Jayakumar, Jean Marie Vianney Nsanzimana, Madhavi Srinivasan, Jinho Choi,* and Jong-Min Lee*

Efficient bifunctional electrocatalysts for oxygen reduction reaction (ORR) and oxygen evolution reaction (OER) are required for metal–air batteries, to replace costly metals, such as Pt and Ir/Ru based compounds, which are typically used as benchmarks for ORR and OER, respectively. Isolated single atomic sites coordinated with nitrogen on carbon supports have promising performance for replacement of precious metal catalysts. However, most of monometallic M-N-C catalysts demonstrate unsatisfactory bifunctional performance. Herein, a facile way of preparing bimetallic Fe and Co sites entrapped in nitrogen-doped hollow carbon nanospheres (Fe,Co-SA/CS) is explored, drawing on the unique structure and pore characteristics of Zeolitic imidazole frameworks and molecular size of Ferrocene, an Fe containing species. Fe,Co-SA/CS shows an ORR onset potential and half wave potential of 0.96 and 0.86 V, respectively, while the values of commercial Pt/C are 0.97 and 0.84 V, respectively. For OER, (Fe,Co)-SA/CS attains its anodic current density of 10 mA cm^{-2} at an overpotential of 360 mV and commercial RuO$_2$ catalyst attains it at 344 mV. Interestingly, the oxygen electrode activity (ΔE) for (Fe,Co)-SA/CS and Pt/C-RuO$_2$ is calculated to be 0.73 V, exhibiting the bifunctional catalytic activity of (Fe,Co)-SA/CS. (Fe,Co)-SA/CS evidences desirable specific capacity and cyclic stability than Pt/C-RuO$_2$ mixture when utilized as an air cathode in a homemade Zinc–air battery. The material shows promising ability to replace precious catalysts in rechargeable metal–air batteries.

Rapid growth of energy sectors has now stimulated high demand for clean and renewable energy storage and conversion technologies like water splitting electrolysers, fuel cells and metal–air batteries.[1–5] Among these technologies, rechargeable metal–air batteries have received much attention due to their high theoretical energy density and long-term stability.[6,7] In addition, the metal anodes like Zn, Al, and Mg, are earth abundant, available in low cost and can be recycled, enabling utilizationfor more practical applications in industrial levels.[8,9] However, rechargeable metal–air batteries require efficient bifunctional electrocatalysts for oxygen reduction reaction (ORR) and oxygen evolution reaction (OER). Nowadays, precious and scarce metal (like Pt and Ir/Ru) based electrocatalysts are used for ORR and OER, respectively, limiting the full-fledged development of metal–air batteries due to high costs.[10–12] Hence, there is an urgent requirement to develop efficient, cheap and durable materials that can act as air cathode and catalyze both charging

V. Jose
Energy Research Institute @ NTU
ERI@N
Interdisciplinary Graduate School Nanyang Technological University
50 Nanyang Drive, Singapore 637553, Singapore
V. Jose, J. M. V. Nsanzimana, J.-M. Lee
School of Chemical and Biomedical Engineering
Nanyang Technological University
62 Nanyang Drive, Singapore 637459, Singapore
E-mail: jmlee@ntu.edu.sg
H. Hu, J. Choi
College of Energy, Soochow Institute for Energy and Materials
Innovations, and Key Laboratory of Advanced Carbon Materials and
Wearable Energy Technologies of Jiangsu Province
Soochow University
Suzhou 215006, China
E-mail: jhchoi@suda.edu.cn

E. Edison, W. Manalastas Jr., H. Ren, M. Srinivasan
School of Materials Science and Engineering
Nanyang Technological University
50 Nanyang Ave, Singapore 639798, Singapore
P. Kidkhunthod
Synchrotron Light Research Institute
Nakhon Ratchasima 30000, Thailand
S. Sreejith
National University of Singapore
14 Medical Drive, Singapore 117599, Singapore
A. Jayakumar
School of GeoSciences
Biochar Research Centre
University of Edinburgh
Edinburgh EH9 3FF, UK

ADVANCED
SCIENCE NEWS
www.advancedsciencenews.com

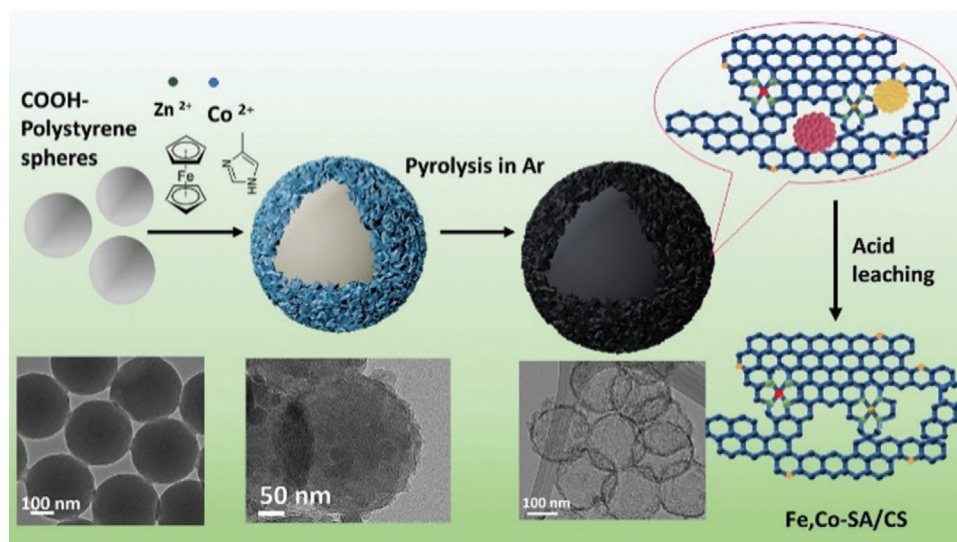small
methods
www.small-methods.com

Figure 1. Schematic process for preparation of Fe,Co-SA/CS.

(corresponding OER) and discharging (corresponding ORR) processes efficiently.

Recently, isolated single atomic sites coordinated with nitrogen on carbon supports, represented as M-N-C (M = Fe, Co, Ni, Cu, etc), were found to have promising performance.[13–16] They can potentially replace precious metal catalysts for either OER and ORR. Apart from the fact that single atomic M-N-C catalysts have high intrinsic activity, they also exhibit advantages, such as high atom utilization, low coordination and high exposure of active sites in contrast to their nanoparticle counterparts.[17–19] Studies have shown that single atoms exhibit superior stability on supporting structures through covalent and electronic interactions.[20,21] Homogeneity of single atomic sites on supporting matrix ensures high selectivity toward a single end product which has high importance in electrocatalysis. However, most of the current monometallic M-N-C catalysts in use have an unsatisfactory performance toward the combined ORR and OER. Thus, there is a great challenge to develop efficient bifunctional ORR/OER electrocatalysts.[22–24] A reasonable solution would be to engineer a N doped carbon matrix with bimetallic single atomic sites such that the performance may be accordingly.[25] Owing to the great challenge associated with isolating and stabilizing single atomic sites from bimetallic species, research in this direction remains unexplored.[26]

Special organic and inorganic structures can anchor metal atoms together to produce atomically dispersed metal sites on carbon frameworks.[27] Among such structures, Zeolitic Imidazole Frameworks (ZIFs) are ordered, self-assembling and porous materials, which can act as a platform for synthesizing carbon frameworks doped with single atomic active sites.[28] Specifically, ZIF-8 (with Zn as metal centre) and ZIF-67 (with Co as metal centre) have attracted much attention in this regard.[29,30] However, limited studies have utilized ZIF-8 and ZIF-67 to engineer diatomic metal catalytic sites. Notably, by taking advantages of similar unit cell parameters and isoreticular structures of ZIF-8 and ZIF-67, they can be further modified to form hybrid structures.[31,32] A variety of hybrid materials

can be developed based on the pore-sizes of ZIFs, which can later be converted to single-atomic sites on carbon through heat treatments.

Herein, we report the preparation of new atomically dispersed binary Fe and Co sites entrapped in nitrogen-doped hollow carbon nanospheres (denoted as Fe,Co-SA/CS). The catalyst was obtained through conduct of a modified procedure via heat treatments and acidic washing of hybrid ZIFs grown on carboxylic polystyrene (COOH-PS) nanospheres. Ferrocene, an Fe containing species with molecular size of 6.4 Å, was incorporated into the hybrid ZIFs, by utilizing the pore size and cavity diameter of ZIF-8 which are 3.4 Å and 11 Å, respectively.[33,34] We envisage that such an approach could prevent washing off Fe sources as well as clustering single atomic Fe sites during the synthesis and pyrolysis process, respectively. Single atomic sites of Co and Fe were identified by X-ray absorption (XAS) and aberration-corrected scanning transmission electron microscopy (AC-STEM) studies. Fe,Co-SA/CS can provide excellent oxygen electrocatalysis with a low overpotential and high electron transfer number in an alkaline electrolyte due to its abundant single atomic active sites, synergetic effects of bimetallic sites and nitrogen doping on the porous carbon frameworks. Additionally, theoretical evaluation was carried out to understand the influence of the single atoms and the importance of coexistence of bimetal single atoms on electrocatalytic activity. For evaluating the new catalyst for practical applications, a rechargeable Zinc–air battery was assembled and tested. The electrochemical characteristics for the catalyst were compared with those for Pt/C+RuO$_2$.

The schematic process for the preparation of Fe,Co-SA/CS is shown in **Figure 1**. It was revealed that carboxylate groups act as a good chelating agent on the surface of polystyrene nanospheres that can interact with metal cations.[35] Hence, Zn^{2+} and Co^{2+} can have initial interactions and form hybrid metal organic frameworks of ZIF-8 and ZIF-67 on polystyrene nanospheres with the help of 2-methyl imidazole. These ZIF structures are known to have unique pore characteristics with a
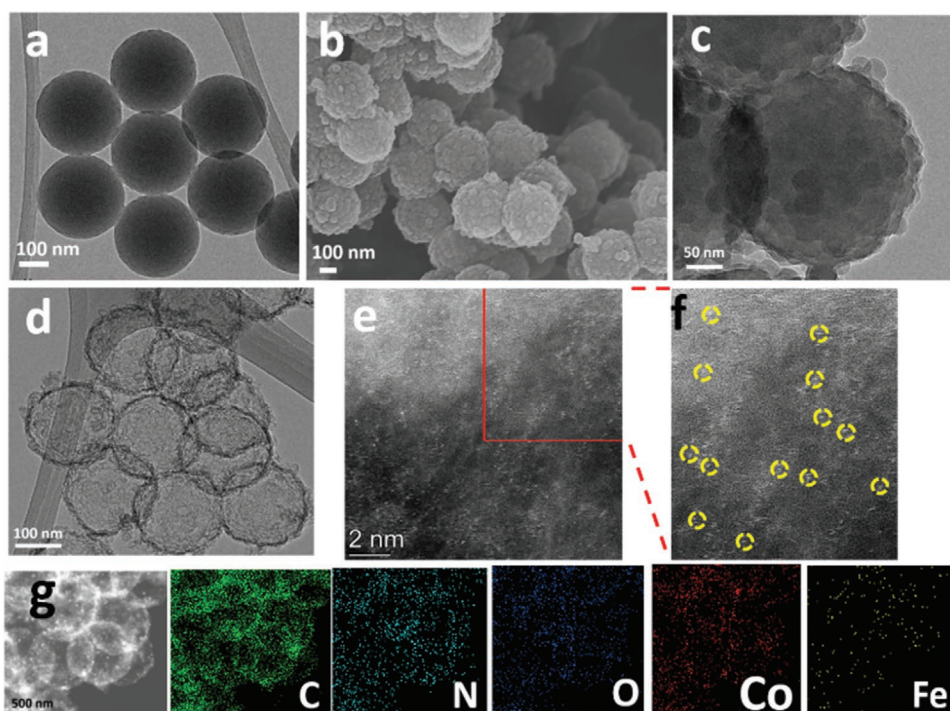
ADVANCED
SCIENCE NEWS
www.advancedsciencenews.com

small
methods
www.small-methods.com

Figure 2. FESEM images of a) Carboxylic polystyrene spheres b) Ferrocene,Co,Zn ZIF/COOH-PS. TEM images of c) Ferrocene,Co,Zn ZIF/COOH-PS d) (Fe,Co)-SA/CS. HAADF-STEM image of showing single atoms dispersed in carbon e,f) (Fe,Co)-SA/CS. g) Elemental mapping of (Fe,Co)-SA/CS.

similar pore size of about 3.4 Å and a cavity diameter of about 11 Å.[33,36] Meanwhile, ferrocene is an iron-containing molecule with a molecular size of 6.4 Å and is easy soluble in methanol where the ZIF particles are prepared.[34] Therefore, ferrocene molecules in methanol allowed for entrapment in cavities of the hybrid ZIF structures with comparable porosity, leading to a successful dispersion of iron content in the hybrid ZIF over the COOH-PS. TEM (**Figure 2**a) and FESEM (Figure S1, Supporting Information) images reveal successful preparation of well-structured PS spheres with a radius of about 150 nm uniformly. Successful growth of hybrid ZIF on PS can be confirmed from FESEM and TEM images shown in Figure 2b,c. It is evident that the hybrid ZIF has uniformly grown over the surface of COOH-PS. After ferrocene was added into the mixture, the structure of the hybrid ZIF/PS remains the same (Figure S2, Supporting Information). Ferrocene-hybrid ZIF/PS was later annealed under Ar atmosphere at 400 °C, resulting in decomposition of polystyrene spheres and formation of hollow cores for the catalyst. Carbonization of the hybrid was achieved through raising temperature to 910 °C, which converts the hybrid ZIF to N doped carbon shells with metallic nanoparticles and single atoms. Subsequent acidic washing removed nanoparticle clusters of uncoordinated metal atoms.

The hollow structure of the final material is well evidenced in Figure 2d. The thickness of the outer carbon shell was about 10 to 15 nm, contributing to enhanced electrochemical properties by effective mass and ion transfer. AC HAADF-STEM images of Fe,Co-SA\CS shown in Figure 2e indicate that the metals are dispersed well in atomic scale (bright dots correspond to metals: Fe and Co, and there are no clusters of nanoparticles).

The crystal structure of the carbonized hybrid ZIF was investigated using XRD. Peaks for the metal and metal oxide nanoparticles were also shown (**Figure 3**a). The XRD patterns for Ferrocene,Co,Zn ZIF/COOH-PS and Co,Zn ZIF/COOH-PS show relative intensities of peaks at $2\theta = 36.5°$ and $44.3°$, matching to (111) plane of CoO and (111) plane of metallic cobalt, respectively.[31,37] However, all the three compounds derived from the hybrid ZIFs showed a peak corresponding to (002) plane of graphitic carbon around 24°-27° (JCPDS# 41–1487).[34] It is also known that Zn components in ZIF-8 form ZnO during the carbonization process. However, the presence of nearby carbon atoms resulted in the reduction of ZnO into Zn. Further increase in temperature vaporized Zn, leading to formation of porous structures and enhancement in activity. It is also worth noticing that no peaks corresponding to Fe components were evidenced due to the low loading of Fe on the surface. The metal oxide and metallic nanoparticles can be removed from the framework by leaching in a strong acidic environment. Herein, we leached the products in 2 M HCl to remove redundant nanoparticles, resulting in only Fe, Co single atomic sites as the active components. The results were analyzed using XRD, which shows only crystal faces for graphitic carbon (Figure 3b).

From Raman spectra of Fe-SA/CS, Co-SA/CS and (Fe,Co)-SA/CS (Figure 3c), it is evident that the relative intensity of D band to G band increases from 0.97 to 0.99 and to 1, respectively, which indicates the lowest graphitization degree and the highest defects in (Fe,Co)-SA/CS. The presence of defective sites can be rationalized to result from the effect of high temperature pyrolysis and etching of metal\metal oxide nanoparticles from the carbon support, creating more pores. Therefore,
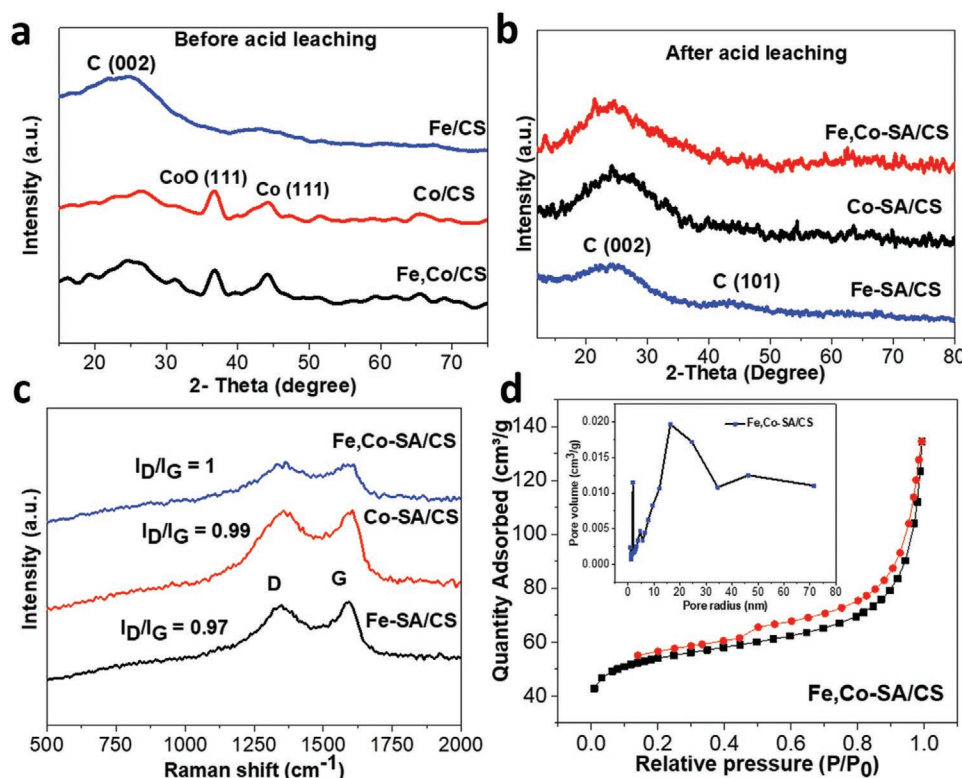
ADVANCED
SCIENCE NEWS
www.advancedsciencenews.com

small
methods
www.small-methods.com

Figure 3. XRD patterns of different catalyst a) before acidic leaching b) after acidic leaching. c) Raman spectra of different catalysts, d) N2 adsorption–desorption isotherms of (Fe,Co)-SA/CS and corresponding pore size distribution is shown in inset.

cobalt and cobalt oxide nanoparticles were removed from the pyrolysis, creating pores on the carbon plane and facilitating better mass transfer. Previous studies have revealed the M-N$_4$ structures are stable at graphitic edges.[38] Hence, the presence of more pores and defective edges on the carbon support can help better coordination of Co and Fe single atoms to nitrogen dopants, which can lead to superior electrocatalytic performances. Hysteresis loops of (Fe,Co)-SA/CS in N$_2$ adsorption–desorption isotherms (Figure 3d) also support the analysis from the Raman spectra, confirming their mesoporous nature. The Brunauer–Emmett–Teller (BET) surface area of (Fe,Co)-SA/CS was found to be 184.57 m^{2}g^{-1}.

X-ray photoelectron spectroscopy (XPS) was utilized to analyze chemical elements and their oxidation states in (Fe,Co)-SA/CS. We detected the presence of C, N, O and Co. Quantitative analysis proves that the amount of O species (4.3%) is much lower than the amount of N species (9.7%). As shown in **Figure 4**a, N 1s spectra of (Fe,Co)-SA/CS can be divided to characteristic peaks centered at 398.2 eV, 400.8 eV and 403.5 eV corresponding to pyridinic N, graphitic N, and oxidized N, respectively.[39,40] According to previous studies, additional peak appearing around 399.3 eV can be assigned to N-coordinated Co or Fe sites like Co(Fe)-N.[41] It is also evident that pyridinic and graphitic N are more dominant in the sample, which is known to favor ORR. They can also anchor Fe and Co single atoms to the carbon structure, making the single atoms stable in the structure. Electron-accepting pyridinic N species can impart some positive charge on adjacent sp^2 hybridized carbon atoms,[42] facilitating reactant adsorption and promoting charge

transfer between reaction intermediates and catalyst surface, thus enhancing OER and ORR kinetics.[6] XPS peaks for Co 2p are centered at 780.1 eV and 795.4 eV corresponding to Co 2p$_{1/2}$ and Co 2p$_{3/2}$ levels, respectively (Figure 4b). However, peaks corresponding to Fe 2p were hardly detected due to the low concentration of Fe, which may be under the XPS detection limit. Inductively coupled plasma optical emission spectrometry (ICP-OES) analysis revealed that in Fe, Co-SA/CS, the content of Co and Fe is 2.08% and 0.08%, respectively.

X-ray absorption spectroscopy (XAS) was conducted on Fe,Co-SA\CS to gain more insights on electronic and coordination environment of Fe and Co. Figure 4c shows Fe K edge – X-ray absorption near-edge structure (XANES) curve of Fe,Co-SA\CS, together with those of the standard samples of Fe foil, Fe$_2$O$_3$, and FeO. The near-edge absorption energy position of Fe,Co-SA\CS is found to be between that of Fe$_2$O$_3$ and FeO, indicating that Fe atoms in Fe,Co-SA\CS have a valence state between +3 and +2. In addition, the finger print peak of Fe,Co-SA\CS around 7113 eV suggests the presence of the square-planar Fe–N$_4$ species.[43] The Fourier transform extended X-ray absorption fine structure (FT-EXAFS) spectrum of Fe,Co-SA\CS (Figure 4d) shows only one prominent peak at 1.51 Å corresponding to Fe-N(C) scattering paths.[43] Generally, peaks around 2.2 Å are considered to result from Fe-Fe coordination. These peaks are absent in the spectrum for Fe,Co-SA\CS, suggesting that Fe is distributed as single atoms in the catalyst.[44] Co-K edge XANES was also conducted for Fe,Co-SA\CS and it was compared with those for Co foil and CoO, to understand the coordination of Co in the catalyst. As shown in Figure S3a (Supporting Information),
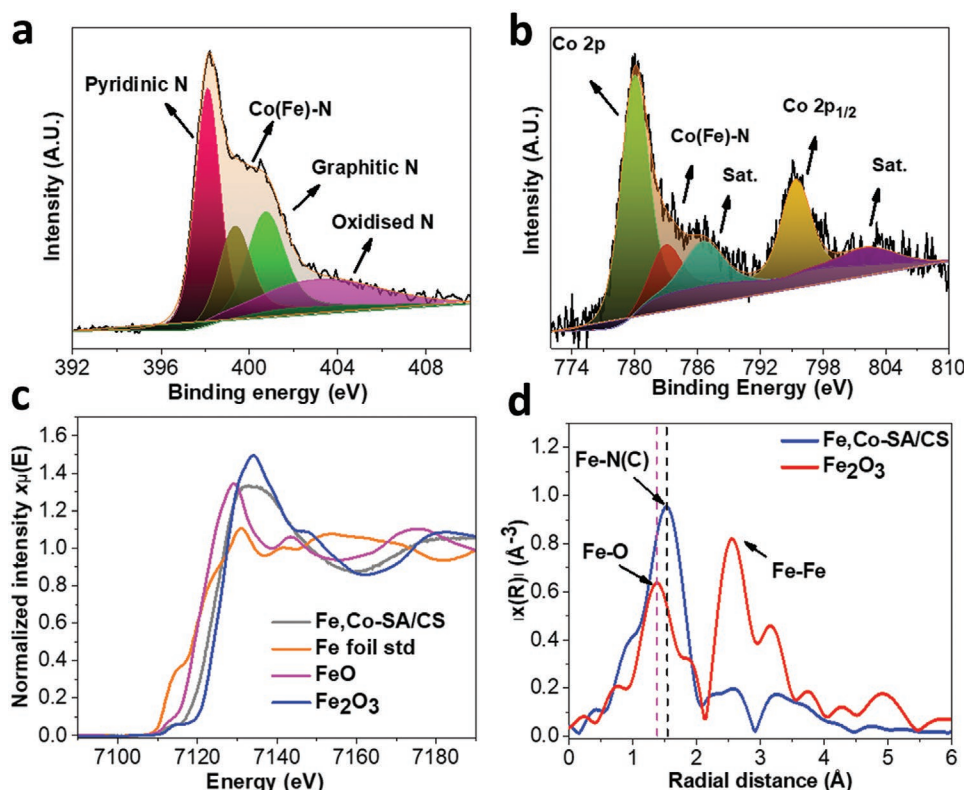
ADVANCED
SCIENCE NEWS
www.advancedsciencenews.com

small
methods
www.small-methods.com

Figure 4. High-resolution XPS spectra of a) N 1s b) Co 2 p in (Fe,Co)-SA/CS. XAS spectra for different samples: c) Fe K-edge XANES spectra and d) FT-EXAFS spectra of (Fe,Co)-SA/CS and Fe_2O_3.

the curve for Fe,Co-SA\CS differs from Co foil, confirming there is no nanocrystalline Co. Pre-edge peak of Fe,Co-SA\CS around 7710 eV is the finger print for Co–N$_4$ square-planar structure, mainly due to the dipole-forbidden 1s → 3d transition with quadrupole coupling.[45,46] FT-EXAFS spectrum for Fe,Co-SA\CS (Figure S3b, Supporting Information) shows only one prominent peak at 1.33 Å corresponding to Co-N(C) scattering paths, which is a little shorter than Co-O peak appearing at 1.53 Å.[47] There is no detectable peak for Fe,Co-SA\CS around 2.2 Å, which corresponds to Co—Co peak in previous studies.[48]

Single atom dispersion is expected to deliver excellent ORR. Thus, the prepared samples were first evaluated for ORR performance using cyclic voltammetry (CV) in a 0.1 M KOH solution. CV curves obtained in a N$_2$ saturated electrolyte in (**Figure 5**a) are mostly featureless, while those conducted in an O$_2$ saturated electrolyte feature well-defined ORR cathodic peaks. When comparing the CV curves between Figure 5a and Figure S4a,b(Supporting Information), it is well evident that (Fe,Co)-SA/CS has the most positive peak potential at 0.85 V, followed by Co-SA/CS (0.84 V) and Fe-SA/CS (0.79 V). To get more insights on their ORR performances, linear sweep voltammetry (LSV) was conducted as shown in Figure 5b. All the three single atom containing samples have good ORR performances and are comparable to commercial Pt/C. In detail, among the prepared samples, (Fe,Co)-SA/CS showed the highest E_{onset} and $E_{1/2}$ (0.96 and 0.86 V) compared with Pt/C (0.97 and 0.84 V), while Co-SA/CS and Fe-SA/CS had E_{onset} and $E_{1/2}$ of (0.94 and 0.83 V) and (0.92 and 0.81 V), respectively. It

is worth noting that, even though (Fe,Co)-SA/CS has a slightly lower onset potential (≈10 mV) compared with Pt/C, it has a higher half wave potential (≈20 mV), elucidating the high ORR activity of (Fe,Co)-SA/CS. The corresponding ORR Tafel slopes (Figure S8a, Supporting Information) also elucidate the high ORR activity of (Fe,Co)-SA/CS. The Fe-Co-SA/C without polystyrene spheres showed poor ORR performance when compared with the hollow samples, elucidating the importance of thin hollow morphology. Moreover, the effect of bimetallic single atoms is evident compared with the performances of the other samples. The corresponding ORR Tafel slopes are given in Figure S8a (Supporting Information). These results are also supported by DFT calculations, which will be discussed later in detail. Figure S5–S7 (Supporting Information) show that diffusion current density increases with an increase in rotation speed for all the catalysts and corresponding Koutecky–Levich (K–L) plots, when calculated with in a potential range of 0.4–0.55 V, show good linearity, suggesting that the ORR kinetics are of first order. Electron transfer number per oxygen molecule (*n*) can be calculated from the K–L equation and it was found to be about 4 for both (Fe,Co)-SA/CS and Co-SA/CS, while it was about 3 for Fe-SA/CS.

To evaluate the bifunctionality of the catalysts for rechargeable Zinc–air battery, OER performance of the catalysts were measured in a 0.1 M KOH electrolyte.[49] For OER, (Fe,Co)-SA/CS attained an anodic current density of 10 mA cm^{-2} at an overpotential of 360 mV, while the state-of-the-art catalyst RuO$_2$ achieved it at 340 mV and Co-SA/CS attained it at 410 mV,
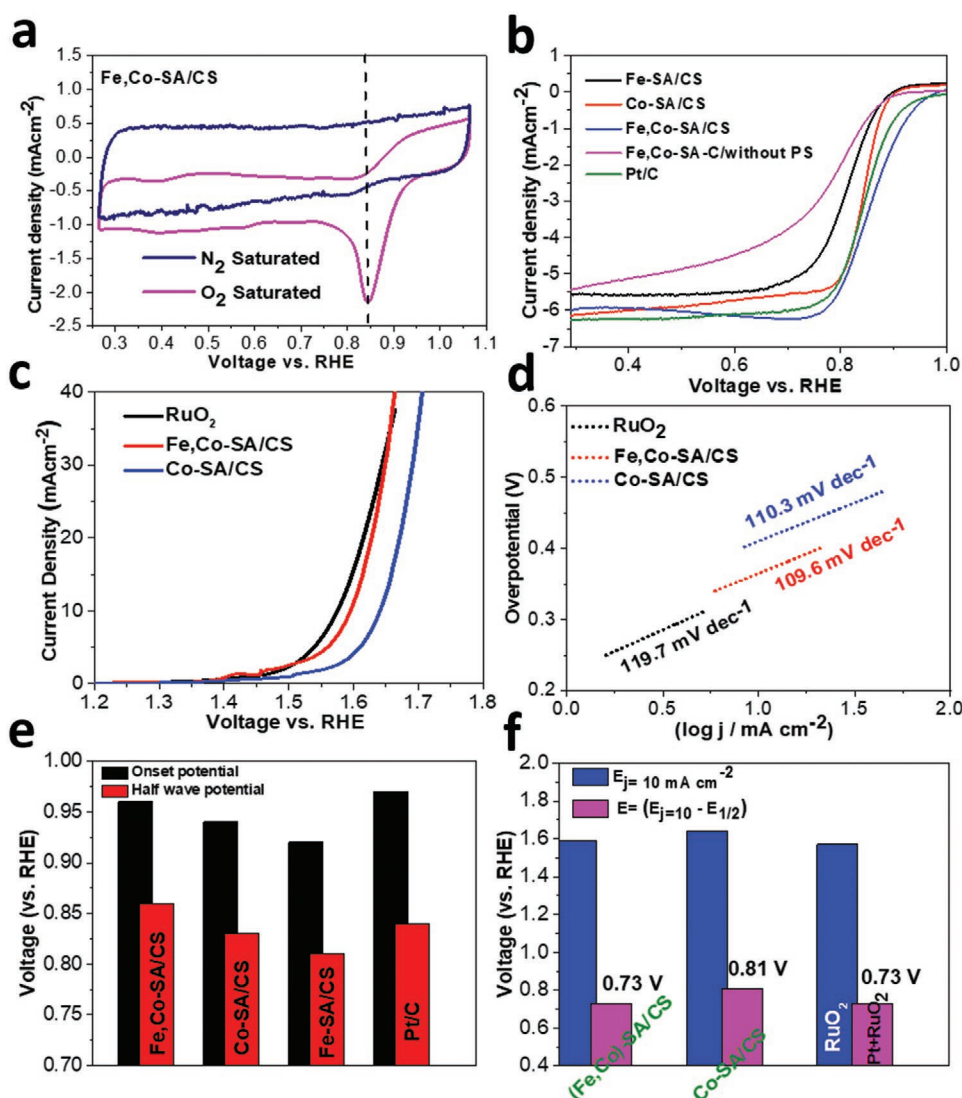
Figure 5. a) CV curves of (Fe,Co)-SA/CS in N_2-saturated and O_2-saturated 0.1 M KOH solution. (5 mV s^{-1}). b) ORR polarization curves of various catalysts in O_2-saturated 0.1 M KOH (rotation rate: 1600 rpm; sweep rate: 5 mV s^{-1}). c) OER polarization curves of various catalysts in O_2-saturated 0.1 M KOH (sweep rate: 5 mV s^{-1}) and d) corresponding derived Tafel slopes. e) Onset potential and half wave potential ($E_{1/2}$) of various catalysts. f) OER potential at a current density of 10 mA cm^{-2} ($E_{j = 10}$) and ΔE ($E_{j = 10} - E_{1/2}$) of different catalysts.

elucidating the superior OER performance of (Fe,Co)-SA/CS in the alkaline medium (Figure 5c, Supporting Information). Tafel slopes of (Fe,Co)-SA/CS and Co-SA/CS also reveal better performance of (Fe,Co)-SA/CS. Overall bifunctional electrocatalytic activity for ORR/OER can be analyzed by calculating oxygen electrode activity (ΔE) from the difference between OER potential required to achieve 10 mA cm^{-2} and ORR half-wave potential. Interestingly, (Fe,Co)-SA/CS has 0.73 V of ΔE, which is same as that of the state-of-the-art catalyst Pt/C-RuO$_2$ ($\Delta E = 0.73$ V). The superior performance of (Fe,Co)-SA/CS can be attributed to synergistic effects of the N-coordinated bimetallic single atoms in the carbon support and the unique structure of carbon with a few nanometer thickness and high density of pores, which are desirable for efficient transport of reaction intermediates. Figure S8 (Supporting Information) shows that (Fe,Co)-SA/CS is stable for b,c) ORR and d) OER in the alkaline medium.

To understand the enhanced ORR/OER activity of (Fe, Co)-SA/CS, we performed density functional theory (DFT) calculations for the doped SA/CS. Here, Fe-SA/CS, Co-SA/CS, and (Fe, Co)-SA/CS were modeled by substituting the C atom of N-doped graphene with dopants (Figure S9, Supporting Information). Oxygen atom and molecule tend to adsorb on the metal dopants.[50,51] There are two possible adsorption sites for (Fe, Co)-SA/CS, Co and Fe sites, and hereafter, the reactions on the Co and Fe sites are denoted as (Fe, Co*)-SA/CS and (Fe*, Co)-SA/CS, respectively. The calculated free energies (G) and the optimized structures of the intermediate states along the reaction pathway for ORR are displayed in **Figure 6** and Figures S10–S13 (Supporting Information), respectively. All the reaction steps are exergonic at $U = 0$ V. The limiting potential (U_{lim}), which is the maximum external potential until which the reactions still remain exothermic, is 0.86 V for (Fe,

ADVANCED
SCIENCE NEWS
www.advancedsciencenews.com

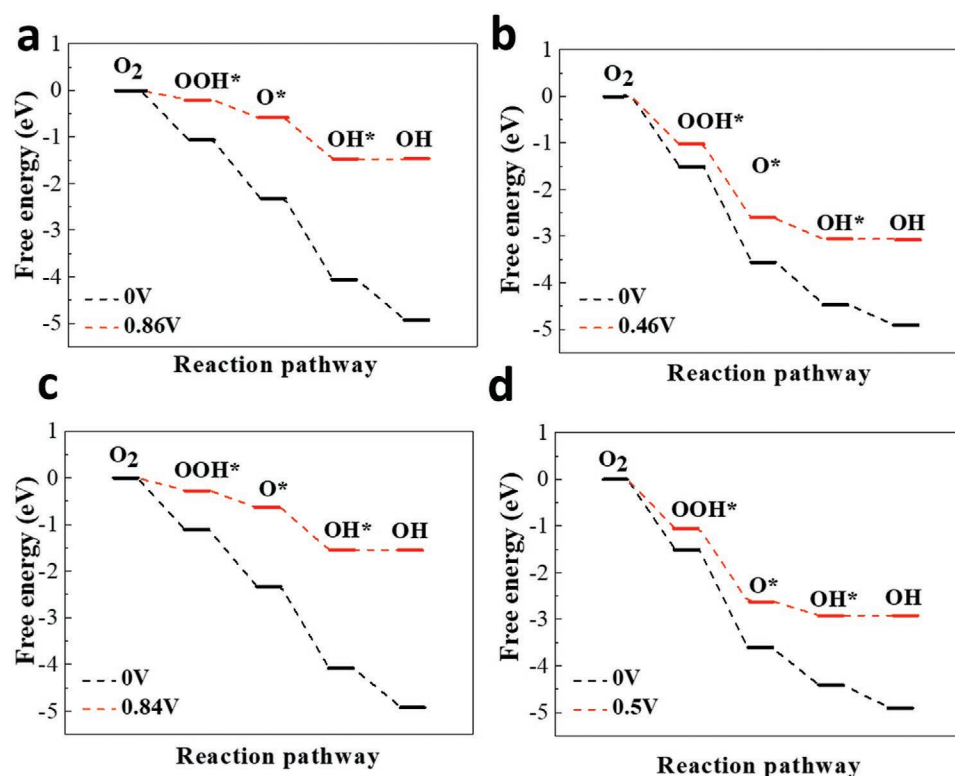small
methods
www.small-methods.com

Figure 6. The free-energy diagrams for ORR: a) (Fe, Co*)-SA/CS, b) (Fe*, Co)-SA/CS, c) Co-SA/CS, and d) Fe-SA/CS. The red line represents the energy profile at the predicted limiting potential.

Co*)-SA/CS, which is higher than 0.5 V of Fe-SA/CS, 0.46 V of (Fe*, Co)-SA/CS, and 0.84 V of Co-SA/CS; all the corresponding limiting steps are the release of OH*. This indicates that (Fe, Co*)-SA/CS can show the best catalytic activity for ORR. Since OER is the reverse process of ORR, all the elementary reactions for OER are endergonic, and U_{lim} can be defined as $U_{lim}(OER) = \max(-\Delta G)/ne - 1.23$ V.[52] The values are in the order of Fe-SA/CS (0.86V) > (Fe*, Co)-SA/CS (0.82 V) > Co-SA/CS (0.52 V) > (Fe, Co*)-SA/CS (0.5 V), where lower values represent better OER performances. These results validate the experimental observation in which (Fe, Co)-SA/CS shows the best catalytic performance for both ORR and OER. Also, these results suggest that the presence of Fe dopants near Co single atoms can influence the performance of electrocatalytic sites, resulting in the enhanced ORR and OER performance.

In order to elucidate the practical application of (Fe,Co)-SA/CS, a homemade rechargeable Zinc–air battery was assembled. Zinc plate was served as the anode. Catalyst coated carbon paper with a loading of 0.5 mg cm^{-2} was served as the cathode. A mixture of 6 M KOH and 0.2 M zinc acetate was used as the electrolyte. A mixture of the state-of-the-art Pt/C (for ORR) and RuO$_2$ (for OER) catalysts was used as a control catalyst in the battery to compare their performances. Battery with (Fe,Co)-SA/CS delivered a stable open circuit voltage (OCV) of 1.43 V for 10 000 s (**Figure 7**a). As shown in polarization curves in Figure 7b,c, discharge current for (Fe,Co)-SA/CS was comparable to that for Pt/C//RuO$_2$ and maximum power density for (Fe,Co)-SA/CS was 86.65 mW cm^{-2}, while that for Pt/C//RuO$_2$ was 110.3 mW cm^{-2}.

(Fe,Co)-SA/CS has a high specific capacity of 819.6 mAh g^{-1}, while Pt/C//RuO$_2$ has only about 779.7 mAh g^{-1} (Figure 7d), clearly demonstrating the ability of (Fe,Co)-SA/CS to function as an efficient air cathode for energy conversion and storage applications. In addition, charging–discharging performance of (Fe,Co)-SA/CS was comparable to that of Pt/C//RuO$_2$. Furthermore, as shown in Figure 7e, the rechargeability and cycling stability for (Fe,Co)-SA/CS and Pt/C//RuO$_2$ were measured at a current density of 5 mA cm^{-2}. Zinc–air battery with (Fe,Co)-SA/CS delivers initial charge and discharge potentials of 1.99 and 1.28 V, with a potential gap of 0.71 V (Figure S14a, Supporting Information). After 100 cycles, the discharge potential drops to 1.15 V and charge potential to 2.03 V. However, after 300 cycle (after 100 h), the discharge potential remains almost same at 1.12 V and charge at 2.03 V (a potential gap of 0.88 V, Figure S14b, Supporting Information), demonstrating the excellent stability of (Fe,Co)-SA/CS as the air cathode for the Zinc–air battery. In contrast, zinc–air battery with Pt/C//RuO$_2$ delivers initial charge and discharge potentials of 1.96 and 1.27 V. After 100 cycle, the discharge potential drastically reduces to 0.94 V and the charge potential to 1.97 (a potential gap of 1.03 V), exhibiting its poor stability. The loss and oxidation of the precious metals in the positive charge potentials are known to be main reasons for the poor stability of Pt/C//RuO$_2$.[38] Zn–air batteries can be connected in series to achieve specific power/energy needs for various applications. As a proof of concept, a red LED bulb (1.8 V) (Figure 7f) was lit continuously for 12 h without any change in the brightness using two Zinc–air batteries with (Fe,Co)-SA/CS.
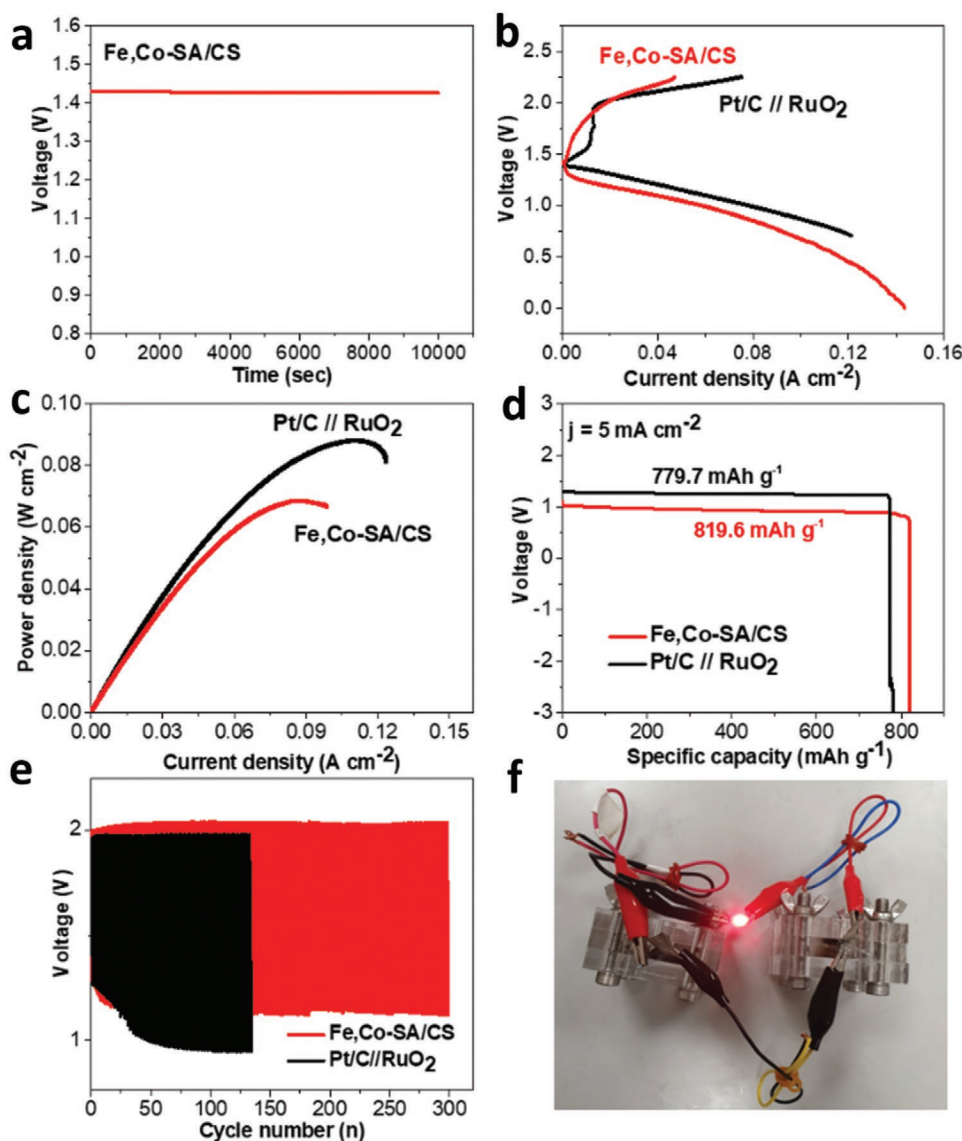
ADVANCED
SCIENCE NEWS
www.advancedsciencenews.com

small
methods
www.small-methods.com

Figure 7. a) Open circuit potential (OCP) of zinc–air battery assembled with (Fe,Co)-SA/CS. b) Polarization curves of (Fe,Co)-SA/CS and Pt/C//RuO2-based Zn–air batteries. c) Power density curves (Fe,Co)-SA/CS and Pt/C//RuO2 based Zn–air batteries derived from corresponding discharge polarization curves. d) Discharge plots of Zn–air batteries catalyzed by (Fe,Co)-SA/CS and Pt/C//RuO2 at a current density of 5 mA cm⁻². e) Long-term discharge–charge performance of (Fe,Co)-SA/CS and Pt/C//RuO2-based Zn–air batteries. f) Photograph of an LED (≈1.8 V) powered by two homemade Zn–air batteries in series with (Fe,Co)-SA/CS as the air cathode.

In summary, we have utilized an electrochemical activation strategy by incorporating Fe single atoms to carbon frameworks consisting of Co single atoms for better ORR and OER performances. The presence of single atomic metallic sites was confirmed by XPS, AC-TEM and XAS analyses. The novel catalyst containing Fe and Co single atomic sites showed an ORR onset potential and half wave potential of 0.96 and 0.86 V, while commercial Pt/C had 0.97 and 0.84 V, respectively. For OER, (Fe,Co)-SA/CS attained its anodic current density of 10 mA cm⁻² at an overpotential of 360 mV and commercial RuO₂ catalyst attained it at 344 mV. The very thin carbon structure consisting of abundant pores is beneficial for mass and ion transfer. The single atoms can anchor to defective sites on the framework to form stable structures, which can play an important role in the long-term stability. Among the prepared catalysts, (Fe, Co)-SA/CS exhibited the best ORR and OER performance. Fe single atomic sites neighboring Co sites may facilitate relatively easy reactant adsorption and charge transfer on Co active sites, which may be the main reason for the enhanced electrocatalytic activity of (Fe, Co)-SA/CS compared with the other catalysts. Benefiting from the excellent bifunctional activity, the newly developed Fe, Co-SA/CS was utilized as the air cathode in a rechargeable Zn–air battery, delivering a stable open circuit potential of 1.43 V with the excellent cycling stability. This work opens a novel avenue to engineer highly efficient multi-metal single atom-based catalysts for noble metal-free electrocatalysis for energy storage and conversion applications.

Experimental Section

Material Preparation: *Preparation of COOH-PS*: Carboxylic polystyrene spheres were synthesized as mentioned in previous literature.[53] Initially, 0.24 g of NaHCO3 was mixed with 200 mL of DI water and refluxed. Later, 1.0 mL of acrylic acid, 10 mL of styrene, and 0.1 g of potassium persulfate were added into the solution. The solution was mixed under a N_2 flow at 70 °C for 8 h and then the temperature was increased to 90 °C for 1 h before cooling down to room temperature. The resulting product was washed using DI water several times and dried at 60 °C overnight.

Ferrocene ZIF/COOH-PS: 300 mg of COOH-PS was sonicated in 30 mL of methanol for 1 h. Later, 59.4 mg of $Zn(NO_3)_2 \cdot 6H_2O$ and 70 mg of Ferrocene were added into the mixture, followed by 30 min of vigorous mixing. Then, 10 mL of 0.2 M 2-methylimidazole (2-MI) solution in methanol was added into the above mixture and stirred for 3 min. After 3 h of aging, the product was collected through centrifugation, washed in methanol, and dried at 60 °C overnight.

Co,Zn ZIF/COOH-PS: 300 mg of COOH-PS was sonicated in 30 mL of methanol for 1 h. Later, 59.4 mg of $Zn(NO_3)_2 \cdot 6H_2O$ and 30 mg of $Co(NO_3)_2 \cdot 6H_2O$ were added into the solution, followed by 30 min of vigorous mixing. Then, 10 mL of 0.2 M 2-methylimidazole (2-MI) solution in methanol was added into the above mixture and stirred for 3 min. After 3 h of aging, the product was collected through centrifugation, washed in methanol and dried at 60 °C overnight.

Ferrocene,Co,Zn ZIF/COOH-PS: 300 mg of COOH-PS was sonicated in 30 mL of methanol for 1 h. Later, 59.4 mg of $Zn(NO_3)_2 \cdot 6H_2O$, 70 mg of Ferrocene, and 30 mg of $Co(NO_3)_2 \cdot 6H_2O$ were added into the solution, followed by 30 min of vigorous mixing. Then, 10 mL of 0.2 M 2-methylimidazole (2-MI) solution in methanol was added into the above mixture and stirred for 3 min. After 3 h of aging, the product was collected through centrifugation, washed in methanol and dried at 60 °C overnight. Fe,Co-SA/C-without PS was prepared without adding the PS spheres.

Fe-SA/CS, Co-SA/CS, Fe,Co-SA/C-without PS, and (Fe,Co)-SA/CS; all the Ferrocene ZIF/COOH-PS, (Co,Zn) ZIF/COOH-PS, (Ferrocene,Co,Zn) ZIF/COOH-PS and without PS were annealed under Ar atmosphere at 400 °C (ramping rate of 2 °C min^{-1}) for 1 h and then at 910 °C (ramping rate of 5 °C min^{-1}) for 2 h, finally allowing to cool to room temperature. The resulting powder was leached in 2 M HCl for 6 h, later washed in DI water till pH became near neutral and dried at 60 °C, to produce Fe-SA/CS, Co-SA/CS and (Fe,Co)-SA/CS, respectively.

Electrochemical Measurements -: *ORR Measurements*: ORR electrochemical measurements were conducted in a CHI 660D workstation coupled with a rotating disk electrode (RDE, Pine) in a three-electrode system. A Pt-sheet was used as the counterelectrode and Ag/AgCl as the reference electrode in the setup. Rotating disk electrode with 4 mm diameter was used as the working electrode and was coated with a synthesized sample. An ink was prepared by mixing 1mg of synthesized sample in 95 µL of ethanol with 5 µL of 5% Nafion solution through sonication. Later, the ink was drop-casted onto glassy carbon electrode and it was allowed to dry in room temperature. The loading was 0.2 mg cm^{-2}. ORR study was conducted through cyclic voltammograms (CV) in O_2 or N_2 saturated 0.1 M KOH solution at a scan rate of 5 mV s^{-1}. Later, RDE measurements were carried out in O_2 saturated 0.1 M KOH solution at a scan rate of 5 mV s^{-1}.

OER Measurements: OER electrochemical measurements were also conducted in a CHI 660D workstation connected with a three-electrode system with Pt sheet and Ag/AgCl electrodes and counter and reference electrodes, respectively. However, the working electrode for OER was prepared by drop-casting the ink (prepared in a similar method to test for ORR) onto Nickel foam with a surface area of 0.25 cm^{-2} and the loading of catalyst was maintained at 0.2 mg cm^{-2}. Linear sweep voltammograms (LSV) were conducted in 0.1 M KOH electrolyte saturated with O_2 and scan rate was fixed at 5 mV s^{-1}.

Zinc–Air Battery Testing: Zn–air battery was tested in a home-made Zn–air cell. Air cathode was made of hydrophilic carbon paper loaded with a catalyst loading of 4 mg cm^{-2}. A polished Zn plate was used as the anode and 6.0 M KOH with 0.2 M $ZnCl_2$ was used as the electrolyte for the test. The performance was tested using a LAND-CT2001A system.

Theoretical Calculation Methods: First-principles DFT calculations were performed using the projector-augmented wave (PAW) method[54] and the Perdew–Burke–Ernzerhof (PBE) exchange correlation functional[55] as implemented in the Vienna Ab-initio Simulation Package.[56,57] The plane-wave set with a cutoff energy of 550 eV was adopted in all calculations. During structural optimization, all the atoms were allowed to relax until the force exerted on each atom was less than 0.02 eV Å^{-1}. The vacuum space of 15 Å at least was selected to avoid the interactions between images. The 2D Brillouin zone was sampled using a $7 \times 3 \times 1$ mesh. The free energies of adsorbates and molecules were obtained by a formula $G = E_{DFT} + ZPE - TS$, where E_{DFT}, ZPE, and S represent the DFT total energy, zero point energy, and entropy, respectively. The temperature T was set to 300 K.

The four-electron pathway, by which the ORR occurs under base condition, is generally reported to proceed according to the following steps

$$O_2 + * \rightarrow O_2* \tag{1}$$

$$O_2* + H_2O + e^- \rightarrow OOH* + OH^- \tag{2}$$

$$OOH* + e^- \rightarrow O* + OH^- \tag{3}$$

$$O* + H_2O + e^- \rightarrow OH* + OH^- \tag{4}$$

$$OH* + e^- \rightarrow OH^- + * \tag{5}$$

The computational hydrogen electrode (CHE) model[58] was used to account for the effect of electrode potential (U) on the free energy of the electron transfer steps: $\Delta G_U = -eU$.

Supporting Information

Supporting Information is available from the Wiley Online Library or from the author.

Conflict of Interest

The authors declare no conflict of interest.

Keywords

[1] J. Anjali, V. K. Jose, J.-M. Lee, *J. Mater. Chem. A* **2019**, *7*, 15491.
[2] D. He, Y. Xiong, J. Yang, X. Chen, Z. Deng, M. Pan, Y. Li, S. Mu, *J. Mater. Chem. A* **2017**, *5*, 1930.
[3] C. Du, L. Yang, F. Yang, G. Cheng, W. Luo, *ACS Catal.* **2017**, *7*, 4131.
[4] P. Prabhu, V. Jose, J.-M. Lee, *Matter* **2020**, *2*, 526.
[5] P. Prabhu, V. Jose, J.-M. Lee, *Adv. Funct. Mater.* **2020**, *30*, 1910768.

[6] C.-Y. Su, H. Cheng, W. Li, Z.-Q. Liu, N. Li, Z. Hou, F.-Q. Bai, H.-X. Zhang, T.-Y. Ma, *Adv. Energy Mater.* **2017**, *7*, 1602420.

[7] D. Stock, S. Dongmo, J. Janek, D. Schröder, *ACS Energy Lett.* **2019**, *4*, 1287.

[8] J. Fu, R. Liang, G. Liu, A. Yu, Z. Bai, L. Yang, Z. Chen, *Adv. Mater.* **2019**, *31*, 1805230.

[9] D. Zhou, Y. Jia, H. Yang, W. Xu, K. Sun, J. Zhang, S. Wang, Y. Kuang, B. Liu, X. Sun, *J. Mater. Chem. A* **2018**, *6*, 21162.

[10] L. An, Z. Zhang, J. Feng, F. Lv, Y. Li, R. Wang, M. Lu, R. B. Gupta, P. Xi, S. Zhang, *J. Am. Chem. Soc.* **2018**, *140*, 17624.

[11] H. Wu, M. Zeng, Z. Li, X. Zhu, C. Tian, C. Xia, L. He, S. Dai, *Sustainable Energy Fuels* **2019**, *3*, 136.

[12] H. Wang, J.-M. Lee, *J. Mater. Chem. A* **2020**, *8*, 10604.

[13] J. Han, X. Meng, L. Lu, J. Bian, Z. Li, C. Sun, *Adv. Funct. Mater.* **2019**, *29*, 1808872.

[14] L. Zhang, Y. Jia, G. Gao, X. Yan, N. Chen, J. Chen, M. T. Soo, B. Wood, D. Yang, A. Du, X. Yao, *Chem* **2018**, *4*, 285.

[15] C. Zhu, Q. Shi, S. Feng, D. Du, Y. Lin, *ACS Energy Lett.* **2018**, *3*, 1713.

[16] Z. Wang, H. Jin, T. Meng, K. Liao, W. Meng, J. Yang, D. He, Y. Xiong, S. Mu, *Adv. Funct. Mater.* **2018**, *28*, 1802596.

[17] W. Zang, A. Sumboja, Y. Ma, H. Zhang, Y. Wu, S. Wu, H. Wu, Z. Liu, C. Guan, J. Wang, S. J. Pennycook, *ACS Catal.* **2018**, *8*, 8961.

[18] H. Zhang, G. Liu, L. Shi, J. Ye, *Adv. Energy Mater.* **2018**, *8*, 1701343.

[19] R. Lang, T. Li, D. Matsumura, S. Miao, Y. Ren, Y. T. Cui, Y. Tan, B. Qiao, L. Li, A. Wang, X. Wang, T. Zhang, *Angew. Chem., Int. Ed.* **2016**, *55*, 16054.

[20] J. Liu, *ACS Catal.* **2017**, *7*, 34.

[21] P. Liu, Y. Zhao, R. Qin, S. Mo, G. Chen, L. Gu, D. M. Chevrier, P. Zhang, Q. Guo, D. Zang, B. Wu, G. Fu, N. Zheng, *Science* **2016**, *352*, 797.

[22] X. Han, X. Ling, D. Yu, D. Xie, L. Li, S. Peng, C. Zhong, N. Zhao, Y. Deng, W. Hu, *Adv. Mater.* **2019**, *31*, 1905622.

[23] G. Fu, J.-M. Lee, *J. Mater. Chem. A* **2019**, *7*, 9386.

[24] X. Yan, P. Prabhu, H. Xu, Z. Meng, T. Xue, J.-M. Lee, *Small Methods* **2020**, *4*, 1900575.

[25] Z. Li, H. He, H. Cao, S. Sun, W. Diao, D. Gao, P. Lu, S. Zhang, Z. Guo, M. Li, R. Liu, D. Ren, C. Liu, Y. Zhang, Z. Yang, J. Jiang, G. Zhang, *Appl. Catal., B* **2019**, *240*, 112.

[26] W. Zhang, Y. Liu, L. Zhang, J. Chen, *Nanomaterials* **2019**, *9*, 1402.

[27] L. Jiao, H.-L. Jiang, *Chem* **2019**, *5*, 786.

[28] T. Sun, L. Xu, D. Wang, Y. Li, *Nano Res.* **2019**, *12*, 2067.

[29] B.-W. Zhang, Y.-X. Wang, S.-L. Chou, H.-K. Liu, S.-X. Dou, *Small Methods* **2019**, *3*, 1800497.

[30] X. Sun, S. Sun, S. Gu, Z. Liang, J. Zhang, Y. Yang, Z. Deng, P. Wei, J. Peng, Y. Xu, C. Fang, Q. Li, J. Han, Z. Jiang, Y. Huang, *Nano Energy* **2019**, *61*, 245.

[31] V. Jose, A. Jayakumar, J.-M. Lee, *ChemElectroChem* **2019**, *6*, 1485.

[32] J. Tang, R. R. Salunkhe, J. Liu, N. L. Torad, M. Imura, S. Furukawa, Y. Yamauchi, *J. Am. Chem. Soc.* **2015**, *137*, 1572.

[33] Y. Ye, F. Cai, H. Li, H. Wu, G. Wang, Y. Li, S. Miao, S. Xie, R. Si, J. Wang, X. Bao, *Nano Energy* **2017**, *38*, 281.

[34] J. Wang, G. Han, L. Wang, L. Du, G. Chen, Y. Gao, Y. Ma, C. Du, X. Cheng, P. Zuo, G. Yin, *Small* **2018**, *14*, 1704282.

[35] H. J. Lee, W. Cho, M. Oh, *Chem. Commun.* **2012**, *48*, 221.

[36] L. E. Kreno, K. Leong, O. K. Farha, M. Allendorf, R. P. Van Duyne, J. T. Hupp, *Chem. Rev.* **2012**, *112*, 1105.

[37] K. Deori, S. Deka, *CrystEngComm* **2013**, *15*, 8465.

[38] C. Tang, B. Wang, H.-F. Wang, Q. Zhang, *Adv. Mater.* **2017**, *29*, 1703185.

[39] Q. Zhou, Z. Zhang, J. Cai, B. Liu, Y. Zhang, X. Gong, X. Sui, A. Yu, L. Zhao, Z. Wang, Z. Chen, *Nano Energy* **2020**, *71*, 104592.

[40] B. Y. Xia, Y. Yan, N. Li, H. Bin Wu, X. W. (David) Lou, X. Wang, *Nat. Energy* **2016**, *1*, 15006.

[41] Y. He, S. Hwang, D. A. Cullen, M. A. Uddin, L. Langhorst, B. Li, S. Karakalos, A. J. Kropf, E. C. Wegener, J. Sokolowski, M. Chen, D. Myers, D. Su, K. L. More, G. Wang, S. Litster, G. Wu, *Energy Environ. Sci.* **2019**, *12*, 250.

[42] P. Chen, T. Zhou, L. Xing, K. Xu, Y. Tong, H. Xie, L. Zhang, W. Yan, W. Chu, C. Wu, Y. Xie, *Angew. Chem., Int. Ed.* **2017**, *56*, 610.

[43] Y. Deng, B. Chi, J. Li, G. Wang, L. Zheng, X. Shi, Z. Cui, L. Du, S. Liao, K. Zang, J. Luo, Y. Hu, X. Sun, *Adv. Energy Mater.* **2019**, *9*, 1802856.

[44] W. Ma, J. Mao, X. Yang, C. Pan, W. Chen, M. Wang, P. Yu, L. Mao, Y. Li, *Chem. Commun.* **2019**, *55*, 159.

[45] L. Zhang, J. M. T. A. Fischer, Y. Jia, X. Yan, W. Xu, X. Wang, J. Chen, D. Yang, H. Liu, L. Zhuang, M. Hankel, D. J. Searles, K. Huang, S. Feng, C. L. Brown, X. Yao, *J. Am. Chem. Soc.* **2018**, *140*, 10757.

[46] X. X. Wang, D. A. Cullen, Y.-T. Pan, S. Hwang, M. Wang, Z. Feng, J. Wang, M. H. Engelhard, H. Zhang, Y. He, Y. Shao, D. Su, K. L. More, J. S. Spendelow, G. Wu, *Adv. Mater.* **2018**, *30*, 1706758.

[47] Z. Du, X. Chen, W. Hu, C. Chuang, S. Xie, A. Hu, W. Yan, X. Kong, X. Wu, H. Ji, L. J. Wan, *J. Am. Chem. Soc.* **2019**, *141*, 3977.

[48] J. Wu, H. Zhou, Q. Li, M. Chen, J. Wan, N. Zhang, L. Xiong, S. Li, B. Y. Xia, G. Feng, M. Liu, L. Huang, *Adv. Energy Mater.* **2019**, *9*, 1900149.

[49] S. Dou, X. Li, L. Tao, J. Huo, S. Wang, *Chem. Commun.* **2016**, *52*, 9727.

[50] M. Jiao, W. Song, K. Li, Y. Wang, Z. Wu, *J. Phys. Chem. C* **2016**, *120*, 8804.

[51] D. Geng, N. Ding, T. S. Andy Hor, Z. Liu, X. Sun, Y. Zong, *J. Mater. Chem. A* **2015**, *3*, 1795.

[52] I. C. Man, H. Su, F. Calle-Vallejo, H. A. Hansen, J. I. Martínez, N. G. Inoglu, J. Kitchin, T. F. Jaramillo, J. K. Nørskov, J. Rossmeisl, *ChemCatChem* **2011**, *3*, 1159.

[53] H. Yu, H. Fan, J. Wang, Y. Zheng, Z. Dai, Y. Lu, J. Kong, X. Wang, Y. J. Kim, Q. Yan, J.-M. Lee, *Nanoscale* **2017**, *9*, 7260.

[54] P. E. Blöchl, *Phys. Rev. B* **1994**, *50*, 17953.

[55] J. P. Perdew, K. Burke, M. Ernzerhof, *Phys. Rev. Lett.* **1996**, *77*, 3865.

[56] G. Kresse, J. Furthmüller, *Phys. Rev. B* **1996**, *54*, 11169.

[57] G. Kresse, D. Joubert, *Phys. Rev. B* **1999**, *59*, 1758.

[58] J. K. Nørskov, J. Rossmeisl, A. Logadottir, L. Lindqvist, J. R. Kitchin, T. Bligaard, H. Jónsson, *J. Phys. Chem. B* **2004**, *108*, 17886.

[59] L. Ma, S. Chen, Z. Pei, Y. Huang, G. Liang, F. Mo, Q. Yang, J. Su, Y. Gao, J. A. Zapien, C. Zhi, *ACS Nano* **2018**, *12*, 1949.

[60] L. Yang, L. Shi, D. Wang, Y. Lv, D. Cao, *Nano Energy* **2018**, *50*, 691.

[61] J. Zhang, M. Zhang, Y. Zeng, J. Chen, L. Qiu, H. Zhou, C. Sun, Y. Yu, C. Zhu, Z. Zhu, *Small* **2019**, *15*, 1900307.

[62] S. Li, C. Cheng, X. Zhao, J. Schmidt, A. Thomas, *Angew. Chem., Int. Ed.* **2018**, *57*, 1856.